Supplementary Information.

Characterization of the new BATCH Teflon chamber and on-line analysis of isomeric multifunctional photooxidation products

Finja Löher[1,2], Esther Borrás[3], Amalia Muñoz[3], Anke Christine Nölscher[1,2]

[1]Department of Atmospheric Chemistry, University of Bayreuth, 95447 Bayreuth, Germany
[2]Bayreuth Center of Ecology and Environmental Research (BayCEER), University of Bayreuth, 95447 Bayreuth, Germany
[3]Fundación Centro de Estudios Ambientales del Mediterráneo (CEAM), 46980 Paterna, Valencia, Spain

Correspondence to: Finja Löher (finja.loeher@uni-bayreuth.de) and Anke C. Nölscher (anke.noelscher@uni-bayreuth.de)

S1 Emission Spectrum of Solar Simulator

S1.1 Photolysis Rates

We calculated the compound-specific photolysis rates theoretically in order to overcome the restriction to compounds with available authentic standards, and to exclude mutual formation and solvent effects associated with the empirical evaluation of a large range of in parts solid photooxidation products. The compound-specific absorption cross sections and quantum yields and the resulting photolysis rates are listed in Table S1. The calculation of the photolysis rate from the emission spectrum and the absorption cross section is illustrated exemplary for H_2O_2 in Fig. S1 (quantum yield = 1).

Table S1: Calculated photolysis rates of the measured photooxidation products and other relevant compounds in the BATCH Teflon chamber. Unless stated otherwise, values apply to T = 298 K. The wavelength ranges for which the photolysis rates were calculated were restricted by the available absorption cross section data, and the recorded emission spectrum of the solar simulator ($\lambda > 262$ nm). If no absorption cross section was available, the photolysis rate was set to zero. If no quantum yield was available, it was set to 1. Whenever available, IUPAC-recommended values were selected. The uncertainty of the photolysis rates is 38 %.

Compound	Absorption cross section / nm range	Quantum yield / molecules photons^{-1}	Photolysis rate / s^{-1}	Note
OCR	250 – 291 (Etzkorn et al., 1999)	1	$7.42\pm2.82\times10^{-6}$	
MCR	250 – 291 (Etzkorn et al., 1999)	1	$7.40\pm2.81\times10^{-6}$	
PCR	250 – 291 (Etzkorn et al., 1999)	1	$1.17\pm0.44\times10^{-5}$	
BOH	220 – 280 (El Dib et al., 2006)	1	$4.60\pm1.75\times10^{-8}$	
ONT	171 – 300 (Shama, 1991)	0.004 (Sandus and Slagg, 1972)	$3.01\pm1.14\times10^{-7}$	
NMB	n.a.	n.a.	n.a.	set to zero
MNT	171 – 301 (Shama, 1991)	0.0008 (Sandus and Slagg, 1972)	$1.77\pm0.67\times10^{-8}$	
BAC	220 – 280 (Roth et al., 2010)	1	$1.33\pm0.51\times10^{-6}$	T = 293 − 357 K
PMC	n.a.	n.a.	n.a.	set to zero
GAL	205 – 335 (Bacher et al., 2001)[a]	0.75 (Bacher et al., 2001)[a]	$1.01\pm0.38\times10^{-5}$	
NCR	320 – 450 (Chen et al., 2011)[a]	0.0001 (Bejan et al., 2006)	$1.93\pm0.73\times10^{-5}$	2-nitro-*p*-cresol, T = 293 K
PAC	251 – 407 (Horowitz et al., 2001)[a]	0.24 (Reed Harris et al., 2016)	$1.49\pm0.57\times10^{-4}$	
BAL	220 – 395 (IUPAC, 2024)[a]	0.29 (Zhu and Cronin, 2000)[a]	$2.52\pm0.96\times10^{-4}$	
GLY	250 – 473 (Volkamer et al., 2005)[a]	$\phi(\lambda)$ (IUPAC, 2024)[a]	$2.57\pm0.98\times10^{-4}$	T = 296 K
MGL	219 – 493 (Meller et al., 1991)[a]	$\phi(\lambda)$ (IUPAC, 2024)[a]	$3.02\pm1.15\times10^{-4}$	T = 296 K
PHB	n.a.	n.a.	n.a.	set to zero
H_2O_2	190 – 350 (IUPAC, 2024)[a] 353 – 410 (Kahan et al., 2012)	1 (IUPAC, 2024)[a]	$1.13\pm0.43\times10^{-5}$	T = 296.0 − 297.4 K
Toluene	115 – 315 (Serralheiro et al., 2015)	1	$3.78\pm1.44\times10^{-7}$	
NO_2	205 – 495 (IUPAC, 2024)[a]	$\phi(\lambda)$ (Troe, 2000)[a]	$2.07\pm0.79\times10^{-2}$	
NO_3	400 – 690 (IUPAC, 2024)[a]	$\phi(\lambda)$ (Johnston et al., 1996)[a]	$3.07\pm1.17\times10^{-1}$	

[a] *IUPAC recommendation.*
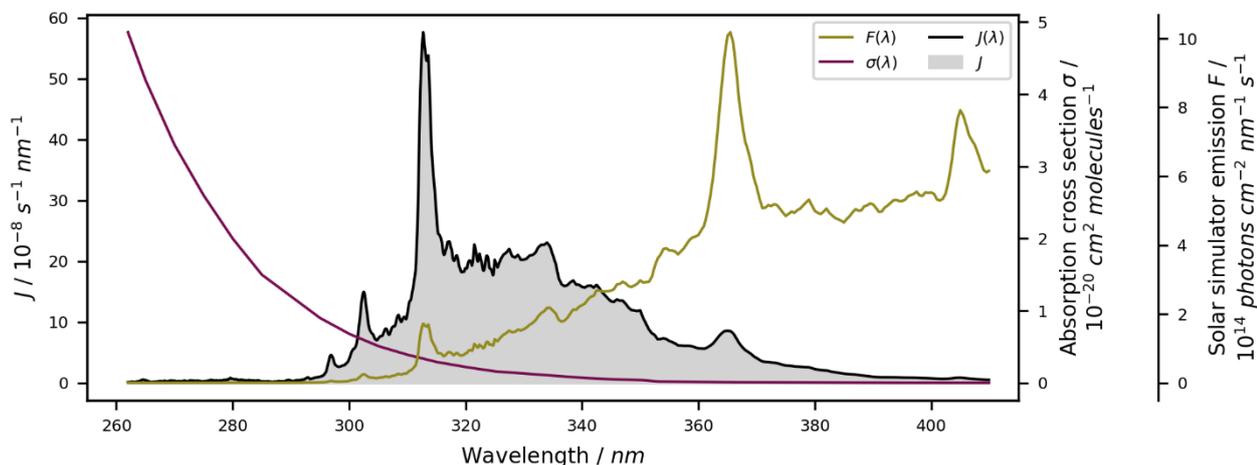
Figure S1: Photolysis of H₂O₂ as a source of OH radicals in the BATCH Teflon chamber. The emission F of the solar simulator, absorption cross section σ of H₂O₂, and resulting photolysis rate J as functions of wavelength are shown. The overall photolysis rate is derived from the integration of the wavelength-specific photolysis rate. The quantum yield of the H₂O₂ photolysis equals unity over the entire wavelength range and is therefore not illustrated specifically.

S1.2 Actinometry

We performed actinometric experiments with NO_2 and methylglyoxal to confirm the emission spectrum that we recorded for the solar simulator.

For the NO_2 chemistry, reactions (R1), (R2), and (R3) need to be considered:

$$NO_2 \overset{h\nu}{\rightarrow} NO + O(^3P) \tag{R1}$$

$$O(^3P) + O_2 \overset{M}{\rightarrow} O_3 \tag{R2}$$

$$NO + O_3 \rightarrow NO_2 + O_2 \tag{R3}$$
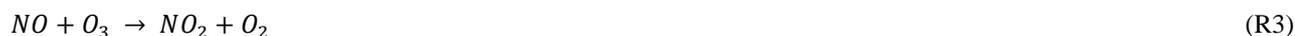
We worked in hydrocarbon-free air to avoid the competitive oxidation of NO by peroxy radicals. During photochemical equilibrium of NO_2, NO, and O_3, the photolysis rate of NO_2 ($J(NO_2)$, s⁻¹) can then be calculated using Eq. (S1):

$$J(NO_2) = \frac{k_{NO+O_3}[NO][O_3]}{[NO_2]} \tag{S1}$$

where k_{NO+O_3} = 1.90±0.31×10⁻¹⁴ molecules⁻¹ cm³ s⁻¹ is the rate constant of the reaction of NO and O_3 at T = 298 K (IUPAC, 2024), and $[NO]$, $[O_3]$, and $[NO_2]$ are the concentrations of NO, O_3, and NO_2 in photostationary state in molecules cm⁻³. Temporal profiles of NO, NO_2, and O_3 in photochemical equilibrium are provided in Fig. S2. The mean values within this time frame were [NO] = 9.38±1.31×10¹¹ molecules cm⁻³, [NO₂] = 1.70±1.41×10¹¹ molecules cm⁻³, and [O₃] = 2.20±0.04×10¹¹ molecules cm⁻³. The error in the resulting NO_2 photolysis rate was calculated from the propagation of the relative errors of the rate constant k, and the concentrations [NO], [NO₂], and [O₃]. It was affected mainly by the high uncertainty in the NO_2 quantification. We derived a value of J = 2.32±1.99×10⁻² s⁻¹ for the NO_2 photolysis rate.

For methylglyoxal, we fitted the wall-loss-corrected decay in the irradiated chamber (Fig. S3). The error in the resulting photolysis rate was calculated from the propagation of the NRMSE of the exponential regression (0.06) and the uncertainty of the assumed wall loss rate (0.14). We derived a value of J = 3.66±0.56×10⁻⁴ s⁻¹ for the methylglyoxal photolysis rate.
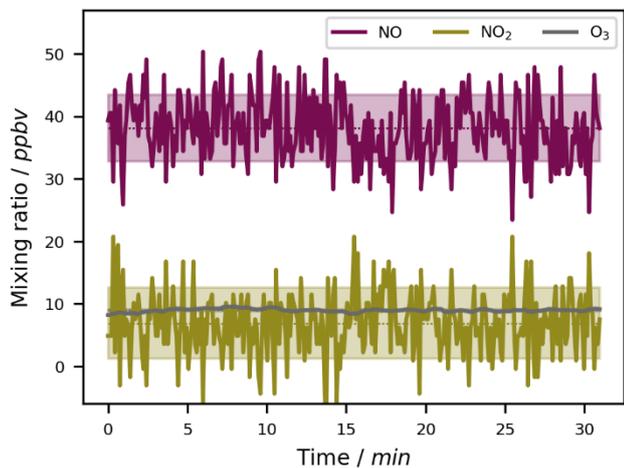
Figure S2: Temporal profiles of NO, NO₂, and O₃ in photostationary state in the BATCH Teflon chamber. The mean values within this time frame were used for the calculation of the NO₂ photolysis rate.
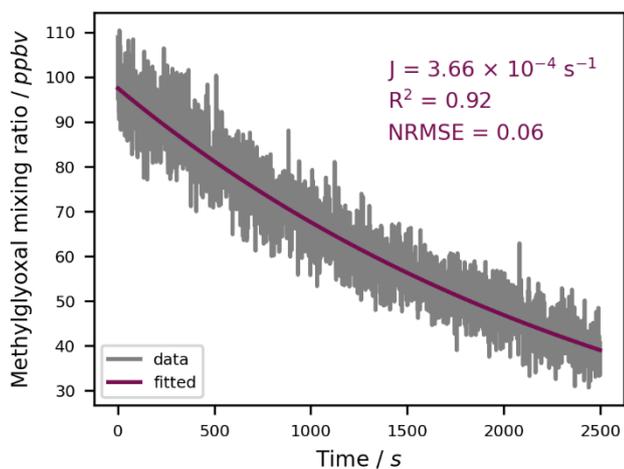
Figure S3: Empirical determination of the methylglyoxal photolysis rate in the BATCH Teflon chamber. The data were obtained on a second resolution over a time frame of roughly 40 minutes. Prior to fitting, the data were corrected for the determined wall loss rate.

S2 Materials

S2.1 Chemicals

The derivatization reagents PFBHA and MSTFA and the catalyst TMCS, as well as the internal standards phenol-d_6 and acetophenone-d_8 were supplied by Sigma Aldrich / Merck (Darmstadt, Germany). Acetonitrile (Roth, Karlsruhe, Germany) and ultrapure water (0.055 µS cm^{-1}) were used as solvents.

The following oxidation products were purchased as authentic standards: *o*-cresol, *m*-cresol, *p*-cresol, benzyl alcohol, *o*-nitrotoluene, *m*-nitrotoluene, *p*-nitrotoluene, (nitromethyl)benzene, benzoic acid, *p*-methylcatechol, glycolaldehyde, 6-nitro-*m*-cresol, benzaldehyde, 40% glyoxal (aq), 40% methylglyoxal (aq), *p*-hydroxybenzaldehyde, acetaldehyde, acetic acid, acetone, formaldehyde, glyoxylic acid, oxalic acid, succinic acid, *p*-toluquinone (Sigma Aldrich / Merck, Darmstadt, Germany), 2-nitro-*p*-cresol, 4-nitro-*m*-cresol, dimethylglyoxal (Thermo Fisher Scientific, Schwerte, Germany), glutaric acid, pyruvic acid (Alfa Aesar, Karlsruhe, Germany), formic acid (Honeywell Fluka, Offenbach, Germany), and methanol (Roth, Karlsruhe, Germany).

S2.2 NO$_x$ and O$_3$ Analysers

A NO$_x$ analyser based on chemiluminescence detection (Teledyne, T200P) was used to monitor NO and NO$_2$. The T200P model is equipped with a high efficiency photolytic converter for NO$_2$ detection. For the NO$_2$ actinometric experiments, we used a CLD 700 AL (ECO PHYSICS). To observe the formation of O$_3$, a UV photometric O$_3$ analyser (Thermo Scientific, 49i) was available. All instruments were calibrated using a dilution calibrator and gas-phase titration (Teledyne, T750U). From the performed calibrations, we derived average noises in the signals of 5.34 ppbv (CLD measurement) and 0.16 ppbv (Blue Light Converter measurement) for NO, 5.73 ppbv (CLD measurement) and 0.12 ppbv (Blue Light Converter measurement) for NO$_2$, and 0.18 ppbv for O$_3$.

S3 SPME-GC-MS Analysis

S3.1 Instrumental Settings

Table S2: GC and MS parameters. Used in this configuration for all tests and experiments conducted in this study.

Step	Parameter
GC inlet	Temperature: 250 °C
	Liner: RESTEK, Topaz, single taper with wool, 23303
	Injection: splitless
GC column	Type: Agilent, HP-5MS, 30 m×0.25 mm×0.25 µm, 19091S-433
	Carrier gas: Helium
	Constant flow: 1.5 sccm
GC oven	Initial temperature: 45 °C, hold 0.1 min
	Ramp 1: 20 °C min^{-1} to 80 °C, hold 2 min
	Ramp 2: 12 °C min^{-1} to 240 °C
	Ramp 3: 100 °C min^{-1} to 280 °C, hold 3 min
MS settings	Transfer line temperature: 280 °C
	Source temperature: 230 °C
	Quadrupole temperature: 150 °C
	Ionization: EI, 70 eV
	Scan mode: m/z 40 – m/z 550, threshold 10, 1562 u s^{-1}
	SIM mode[a]: 3 time segments, dwell times 800 – 900 ms

[a] *See Table 1 in main text.*

Table S3: List of steps in each SPME-GC-MS sampling cycle in chronological order. The double derivatization scheme with the optimized reagent preparation and extraction parameters was adapted from Borrás et al. (2021).

SPME fibre	Instrument
	PFBHA headspace generation
	(Agitator: 50 °C, 500 rpm, 3 min)
PFBHA extraction	
(4 min)	
Sample extraction	MSTFA/TMCS headspace generation
(5 min, 5 SLPM)	(Agitator: 50 °C, 500 rpm, 3 min)
MSTFA/TMCS extraction	
(3 min)	
Desorption into GC inlet	
(250 °C, 40 mm depth, 10 min)	GC-MS run
Fibre conditioning in N$_2$	(20.5 min)
(240 °C, 10 min)	

S3.2 Sampling Cell

The sampling cell consisted of a 126×28×25 mm PTFE block which was held in place by a polyvinylchloride (PVC) body that fitted tightly in the SPME-GC-MS sample tray. A circular hole (9 mm diameter) was drilled through the entire length of the PTFE block to guide the flow of air. The material and the enforced flow profile were designed to reduce species conversions and wall losses. Another hole was drilled from the top so that it connected with the main tunnel. It was sealed with a septum (Supelco, PTFE/silicone, 1.5 mm thickness, 27511) and used as needle guide for the SPME system. During on-line analysis, the fibre coating was placed directly in the sample flow path (penetration depth of 47.5 mm) for maximum extraction efficiency. A technical drawing of the sampling cell is shown in Fig. S4.
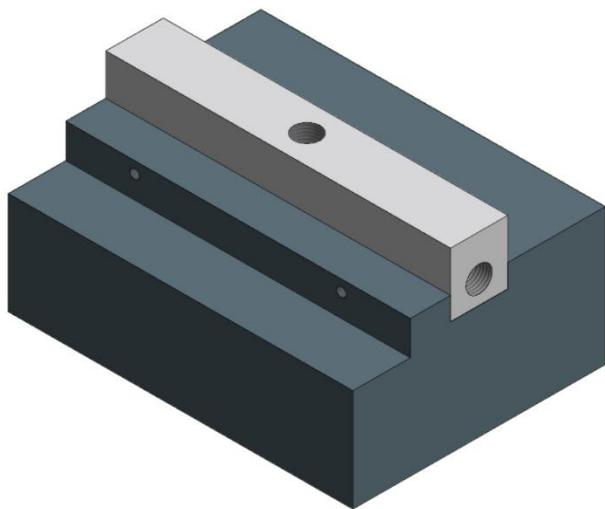
Figure S4: Technical drawing of the sampling cell as illustrated and used for construction by the workshop of the University of Bayreuth. The dark grey area is the PVC body, while the light grey area is the PTFE flow guide. The PTFE part has ¼'' NPT fittings on each side as well as on the top, the latter of which is used to guide the SPME needle into the flow of sample air.

S3.3 Internal Standards

The addition of the ISTDs into the transfer line flow towards the SPME-GC-MS sampling cell was facilitated by means of a customized permeation source (Fig. S5). Permeation sources, in which the pure analyte is slowly released through a permeable layer, are known to supply low concentrations of gases in a constant manner over time if the temperature and flows are carefully controlled (Mitchell, 2000; Namies´nik, 1984; Thorenz et al., 2012). Here, a separate permeation tube was constructed for each ISTD by placing the pure substance in a 2 mL glass vial with open screw cap. For the more volatile acetophenone-d_8, a virginal PTFE septum (thickness: 0.5 mm) was inserted directly in the screw cap (opening 6 mm in diameter). For phenol-d_6, a much larger permeable area was created by placing a 6.5 cm long PTFE tube (outer diameter = 6 mm, inner diameter: 4 mm) tightly through the screw cap and sealing the upper end with a solid PTFE stopper. Both permeation tubes were placed in a 250 mL glass impinger which was continuously flushed with 200 sccm N_2. The outflow was directed either into the main transfer line (for analysis) or into the fume hood (inactive periods). For controlling the temperature, the impinger was wrapped with electric heating wire, insulated rigorously, and placed in a dewar. The voltage of the heating wire was adjusted to achieve a response of the ISTDs similar to the response of the analytes, resulting in about 40 °C in the impinger.
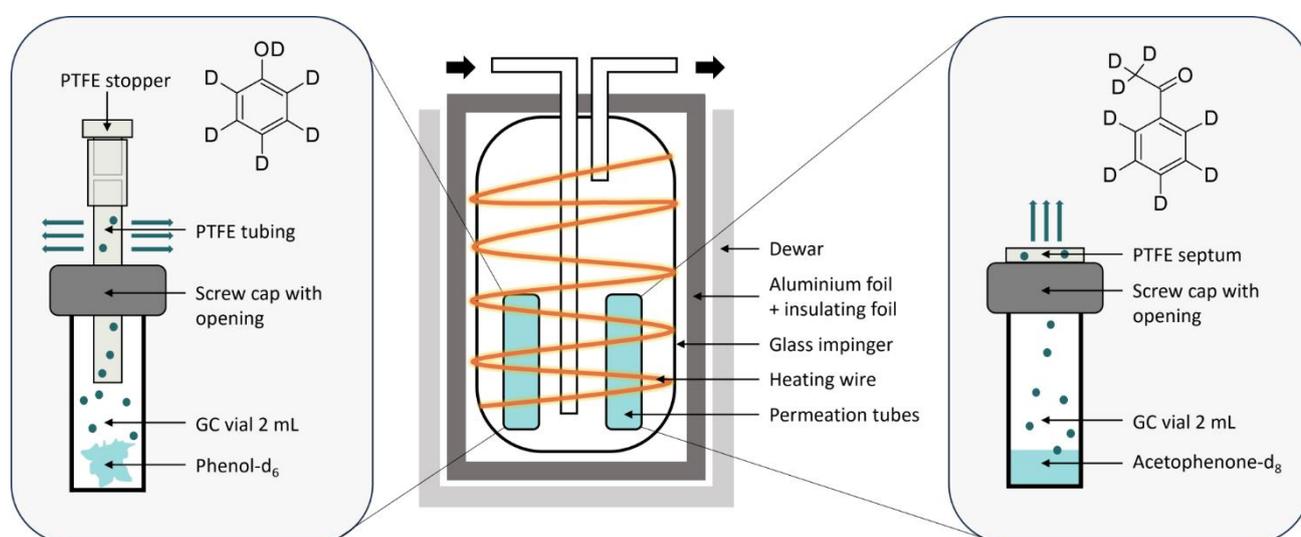
Figure S5: Permeation system for on-line internal standard addition. Customized permeation tubes were designed for phenol-d_6 and acetophenone-d_8. Phenol-d_6 permeated through a PTFE tube (wall thickness 1 mm, 6.5 cm long), while acetophenone-d_8 permeated through a PTFE septum in the open screw cap (thickness 0.5 mm, 6 mm diameter). Both permeation tubes were kept at a constant temperature in an insulated impinger (T = 40 °C) and added with a constant flow of N_2 (200 sccm). Dimensions are not to scale.

S3.4 Derivatization

The silylation of alcohols and carboxylic acids with MSTFA and the typical fragments in the EI spectrum are shown in Fig. S6. Derivatization with MSTFA causes a mass-shift of the analyte to m/z = M+72, due to the addition of the trimethylsilyl (TMS) group with mass 73, and the abstraction of one H atom. Typical losses of TMS adducts upon EI fragmentation include the TMS group $Si(CH_3)_3$ (m/z = 73), CH_3 (m/z = 15), and $Si(CH_3)_3O$ (TMS-O, m/z = 89). The remaining molecular ions have masses of m/z = M-1, m/z = M+57, and m/z = M-17, respectively (Borrás et al., 2021; Jaoui et al., 2004; Lai and Fiehn, 2018; Šepič and Leskovšek, 1999). The TMS ion is often the base ion with the strongest response.

The formation of oximes from ketones and aldehydes with PFBHA and the typical fragments in the EI spectrum are shown in Fig. S7. An intact mono-derivative after reaction with PFBHA will shift to m/z = M+195 (addition of PFBHA with mass 213, and loss of H_2O with mass 18). EI fragmentation produces a range of PFBHA-specific ions. Typically, a strong signal is observed for m/z = 181, resulting from cleavage of the C-O bond. The counterpart of this fragment has a mass of m/z = M+14 compared to the original compound. Other fragmentation mechanisms include O-N cleavage, N-C cleavage, and loss of NO, resulting in fragment ions of m/z = 197 and m/z = M-2, m/z = 211 and m/z = M -16, as well as m/z = 30 and m/z = M+165 respectively (Borrás et al., 2021; Šepič and Leskovšek, 1999). Compounds with multiple carbonyl functional groups can be derivatized multiple times. Given that the side chains of the central carbon atom differ from each other, PFBOs typically exist as geometric cis and trans isomers due to the C=N double bond of the oxime (Borrás et al., 2021; Jang and Kamens, 1999). The chromatogram therefore contains 2^x peaks, where x is the number of stereocentres as induced either by the derivatization process or the molecular structure itself.

Table S4: Number and selection of chromatographic peaks, and mass shifts of the compounds monitored by SPME-GC-MS. The mass shift was calculated as the difference of the evaluated SIM ions compared to the molecular weight. If no further explanation is given, the mass shift represents a typical fragment of the derivatization procedure (see Fig. S6 and S7).

Compound	Peaks (selected)	MW / g mol^{-1}	SIM / m/z	Mass shift	Note
PHE-d$_6$	1	100.15	156.1	M+56	As the TMS replaces a D atom and not a H atom, the mass shift after derivatization is only +71
OCR	1	108.14	165.1	M+57	
MCR	1	108.14	165.1	M+57	
PCR	1	108.14	165.1	M+57	
BOH	1	108.14	135.1	M+27	Loss of all three methyl groups from the TMS group
ONT	1	137.14	91.1	[no derivatization]	C_7H_7 fragment from loss of NO_2
NMB	1	137.14	91.1	[no derivatization]	C_7H_7 fragment from loss of NO_2
MNT	1	137.14	137.1	[no derivatization]	
BAC	1	122.12	179.1	M+57	
PMC	1	124.13	268.1	M+72+72	
GAL	2 (1+2)	60.05	312.1	M+195+57	Both derivatization steps; Peaks overlap, hence evaluated as sum
NCR	1	153.14	210.1	M+57	
PAC	1	88.06	340.1	M+195+57	Both derivatization steps
APH-d$_8$	2 (1)	128.20	323.1	M+195	
BAL	2 (1)	106.12	301.1	M+195	
GLY	2 (1)	58.04	448.1	M+195+195	
MGL	4 (3)	72.06	265.1	M+193	Both carbonyl groups derivatized, one undergoes O-N scission (-2)
PHB	2 (2)	122.12	389.1	M+195+72	Both derivatization steps
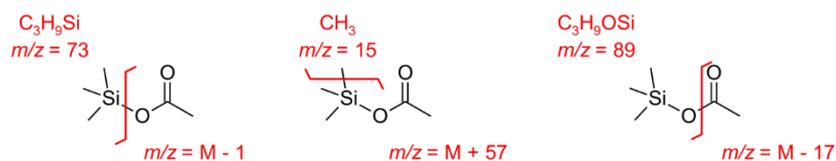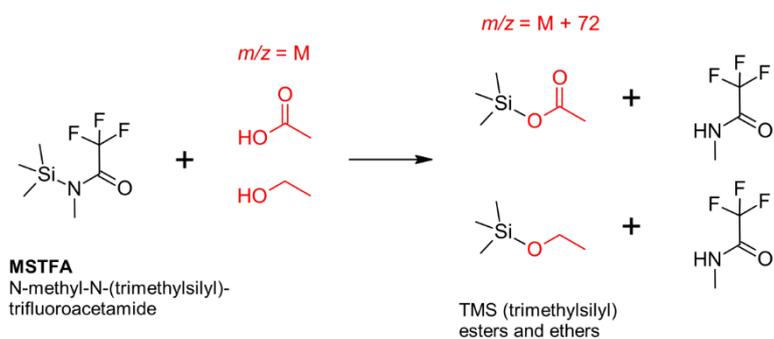
Figure S6: Derivatization mechanism of hydroxy and carboxylic groups and subsequent fragmentation patterns. Upper graph: derivatization of carboxylic acids (top) and alcohols (bottom) by reaction with MSTFA. Lower graph: typical fragments of TMS adducts after electron ionization.
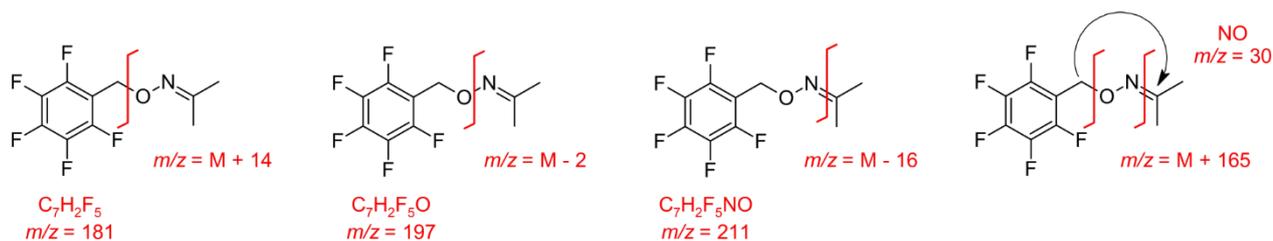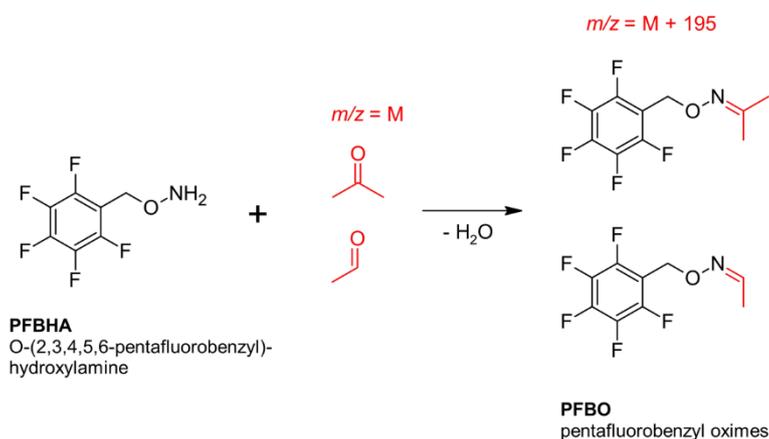
Figure S7: Derivatization mechanism of carbonyls and subsequent fragmentation patterns. Upper graph: derivatization of ketones (top) and aldehydes (bottom) by reaction with PFBHA. Lower graph: typical PFBO fragments after electron ionization.

S4 PTR-ToF-MS Analysis

Table S5: Measurement of toluene, its calibrated photooxidation products, and the internal standards with the PTR-ToF-MS. The primary ion was H_3O^+ in all cases. For all compounds, the sum formula, non-ionized mass, mass after proton transfer, and selected peak are listed. The internal standards were only monitored in a separate measurement to evaluate the stability of the permeation source.

Compound(s)	Sum formula	MW / g mol^{-1}	Protonated mass / m/z	Selected peak / m/z
Glyoxal	$C_2H_2O_2$	58.04	59.01	59.0041
Methylglyoxal	$C_3H_4O_2$	72.06	73.03	73.0243
Toluene, ^{13}C isotope	$^{13}CC_6H_8$	93.13	94.07	94.0716
Benzaldehyde	C_7H_6O	106.12	107.05	107.0470
Cresol isomers + Benzyl alcohol	C_7H_8O	108.14	109.07	109.0626
Phenol-d$_6$[a]	C_6D_6O	100.15	101.09	100.0795[b]
Acetophenone-d$_8$[a]	C_8D_8O	128.20	129.12	129.1172

[a] *Internal standard: not monitored during experiments, not calibrated.*

[b] *The mass m/z -1 had a higher sensitivity than the protonated mass because of hydrogen-deuterium-exchange.*

Table S6: Calibration factors, errors, and LODs for the compounds calibrated for the PTR-ToF-MS. The uncertainty of the slope is derived from the standard error of the slope with a 95% confidence interval. The instrumental error (Instr. Err.) is the mean RSD of all calibration levels. The quantification error (Quant. Err.) includes the instrumental error, the calibration error, and the experimental error. All errors are relative. For the C_7H_8O isomers, we derived a weighted sensitivity by multiplying the recorded sensitivity with the relative abundance as determined by SPME-GC-MS. The weighted calibration factor for the sum signal was obtained from the sum of these weighted isomer-specific sensitivities. When evaluating individual C_7H_8O isomers, we adopted the error and LOD of the weighted sum of the isomers.

Compound(s)	Slope / ncps ppbv^{-1}	Instr. Err. / %	Quant. Err. / %	LOD / pptv
Glyoxal	0.04±0.22	89	91	1827.8
Methylglyoxal	14.42±2.07	2	21	4.8
Benzaldehyde	30.82±2.01	1	21	0.5
Cresol isomers + Benzyl alcohol (averaged)	27.61±1.57	1	21	1.1
Cresol isomers + Benzyl alcohol (weighted)	40.70±1.63	1	21	0.7
o-Cresol (raw / weighted)	49.82±1.72 / 35.37±1.22			
m-Cresol (raw / weighted)	43.52±1.68 / 1.74±0.07			
p-Cresol (raw / weighted)	17.09±1.64 / 3.59±0.34			
Benzyl alcohol (raw / weighted)	0.00 / 0.00[a]			
Glyoxal fragment, *m/z* 31.0145[b]	2.45±1.44			
Benzyl alcohol fragment, *m/z* 91.0522[b]	29.24±2.20			

[a] *No signal on m/z 109.0626 – regression resulted in slightly negative slope, therefore set to zero.*

[b] *Listed here only as information for the reader.*

S5 Loss Corrections

S5.1 Correction Principle
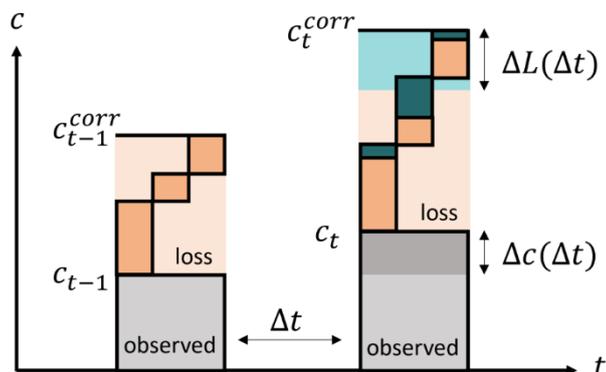
Figure S8: Implementation of the loss corrections. For a given data point, the loss-corrected concentration is calculated as the sum of the loss-corrected concentration of the previous data point, the measured change in concentration, and the absolute loss over that time period. This is equivalent to the measured concentration at that point in time plus the cumulative loss since the beginning of the experiment.

S5.2 Rate Constants for Reactions with OH Radicals

Table S7: Second order rate constants of the reactions of the measured photooxidation products with OH radicals at T = 298 K. Whenever available, IUPAC-recommended values were selected. Here, approximate pseudo first order rate constants (k′) are given as information for the reader to compare the order of magnitude against wall losses and photolysis rates. These rates were calculated with [OH] = 4.89×10^6 molecules cm^{-3} (mean value in experiments at T = 298±1 K in absence of NO$_x$). For the actual implementation of the loss corrections, experiment- and time-specific OH radical concentrations were considered. OH radical concentrations were obtained by evaluating the loss of toluene. The uncertainty of the pseudo first order rate constants is 19 %.

Compound	k(OH) / molecules^{-1} cm^3 s^{-1}	Note	k' / s^{-1}
OCR	4.1×10^{-11} (IUPAC, 2024)[a]		$2.01\pm0.38\times10^{-4}$
MCR	5.9×10^{-11} (IUPAC, 2024)[a]		$2.89\pm0.55\times10^{-4}$
PCR	4.9×10^{-11} (IUPAC, 2024)[a]		$2.40\pm0.46\times10^{-4}$
BOH	2.7×10^{-11} (Harrison and Wells, 2009)[a]		$1.32\pm0.25\times10^{-4}$
ONT	1.22×10^{-12}	MNT value	$5.97\pm1.13\times10^{-6}$
NMB	1.22×10^{-12}	MNT value	$5.97\pm1.13\times10^{-6}$
MNT	1.22×10^{-12} (Atkinson et al., 1989)[a]		$5.97\pm1.13\times10^{-6}$
BAC	1.28×10^{-10} (Wu et al., 2017)		$6.27\pm1.19\times10^{-4}$
PMC	1.5×10^{-10} (Olariu et al., 2000)[a]		$7.34\pm1.39\times10^{-4}$
GAL	8×10^{-12} (IUPAC, 2024)[a]		$3.92\pm0.74\times10^{-5}$
NCR	5.15×10^{-12}	Mean of 2-nitro-*p*-cresol and 6-nitro-*m*-cresol, both (Bejan et al., 2007)[a]	$2.52\pm0.48\times10^{-5}$
PAC	1.2×10^{-13} (Mellouki and Mu, 2003)		$5.87\pm1.12\times10^{-7}$
BAL	1.26×10^{-11} (IUPAC, 2024)[a]		$6.17\pm1.17\times10^{-5}$
GLY	9.7×10^{-12} (IUPAC, 2024)[a]		$4.75\pm0.90\times10^{-5}$
MGL	1.3×10^{-11} (IUPAC, 2024)[a]		$6.36\pm1.21\times10^{-5}$
PHB	1.13×10^{-10} (US EPA, 2024)	Estimated using EPISUITE AopWinv1.92	$5.53\pm1.05\times10^{-4}$

[a] *IUPAC recommendation.*

S5.3 Wall Losses

Table S8: Empirical and fitted wall loss rates of the measured photooxidation products in the BATCH Teflon chamber. The uncertainty of the empirical wall loss rates was derived from the NRMSEs of the individual exponential regressions. The uncertainty of the fitted wall loss rates was calculated according to the 14 % error of the parameterization. The relative change (RC) from the empirical (EMP) to the fitted (FIT) rate was calculated as RC = (FIT − EMP)/EMP. The values for the compound groups are given as mean ± standard deviation of all compounds belonging to this group.

Compound	Group	Wall loss empirical			Wall loss fitted	
		Loss rate / s^{-1}	R^2	Uncertainty / %	Loss rate / s^{-1}	RC / %
OCR	(a)	$3.44\pm0.93\times10^{-5}$	0.57	27	$3.43\pm0.48\times10^{-5}$	±0
MCR	(a)	$3.39\pm0.81\times10^{-5}$	0.65	24	$4.03\pm0.56\times10^{-5}$	+19
PCR	(a)	$4.11\pm0.77\times10^{-5}$	0.76	19	$4.26\pm0.60\times10^{-5}$	+4
BOH	(a)	$4.45\pm0.92\times10^{-5}$	0.73	21	$4.43\pm0.62\times10^{-5}$	±0
ONT	(b)	$1.47\pm0.11\times10^{-5}$	0.96	8	-	-
NMB	(b)	$2.01\pm0.23\times10^{-5}$	0.91	11	-	-
MNT	(b)	$2.24\pm0.31\times10^{-5}$	0.88	14	-	-
BAC	(c)	$7.10\pm1.14\times10^{-5}$	0.82	16	$6.40\pm0.90\times10^{-5}$	-10
PMC	(c)	$8.49\pm1.20\times10^{-5}$	0.86	14	$6.05\pm0.85\times10^{-5}$	-29
GAL	(d)	$4.20\pm0.90\times10^{-5}$	0.70	21	$5.43\pm0.76\times10^{-5}$	+29
NCR	(e)	$6.58\pm1.04\times10^{-5}$	0.83	16	$6.44\pm0.90\times10^{-5}$	-2
PAC	(d)	$5.14\pm0.87\times10^{-5}$	0.78	17	$5.04\pm0.71\times10^{-5}$	-2
BAL	(f)	$4.54\pm1.80\times10^{-6}$	0.07	40	$1.49\pm0.21\times10^{-5}$	+229
GLY	(f)	$1.33\pm0.38\times10^{-5}$	0.45	28	$1.43\pm0.20\times10^{-5}$	+7
MGL	(f)	$1.96\pm0.63\times10^{-5}$	0.35	32	$7.82\pm1.09\times10^{-6}$	-60
PHB	(c)	$8.53\pm0.68\times10^{-5}$	0.95	8	$6.24\pm0.87\times10^{-5}$	-27
(a) Monohydric aromatic alcohols					$4.04\pm0.38\times10^{-5}$	
(b) Nitro compounds		$1.90\pm0.32\times10^{-5}$				
(c) Aromatic acids and multifunctional					$6.23\pm0.14\times10^{-5}$	
(d) Aliphatic multifunctional					$5.23\pm0.19\times10^{-5}$	
(e) Nitro compounds with OH group					6.44×10^{-5} s^{-1}	
(f) Carbonyls and dicarbonyls					$1.23\pm0.32\times10^{-5}$	

S6 SPME-GC-MS Method Evaluation

S6.1 Inter-Sample Variability
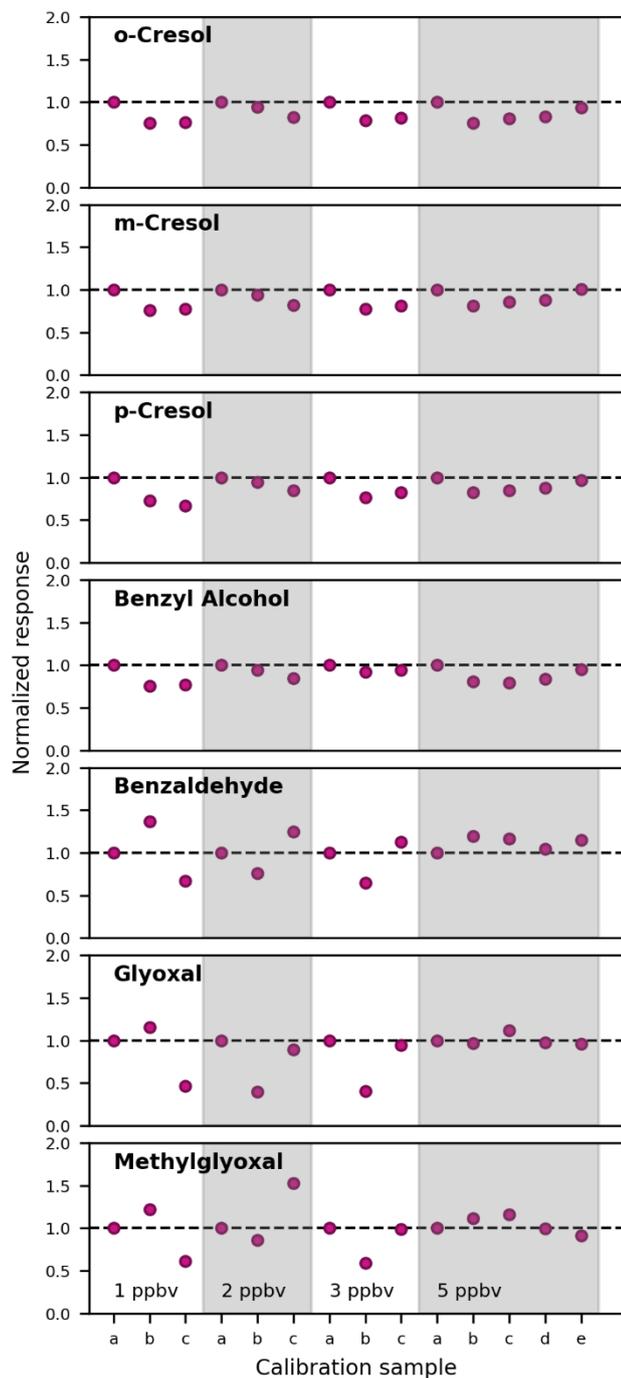
Figure S9: Inter-sample variability of the cresols, benzyl alcohol, benzaldehyde, glyoxal, and methylglyoxal at the SPME-GC-MS. The data are shown for the on-line calibration samples, and normalized within each calibration level. The calibration levels were calculated as concentrations, but are shown here as mixing ratios for simplicity. The depicted data include corrections for internal standard responses, blanks, and wall losses. Note that before each calibration level, the chamber was cleaned, and blanks were recorded (not shown here). The calibration levels at 0 ppbv and 0.5 ppbv are not shown here because of the substantial variability at low concentrations.

S6.2 Derivatization Reagents and Internal Standards
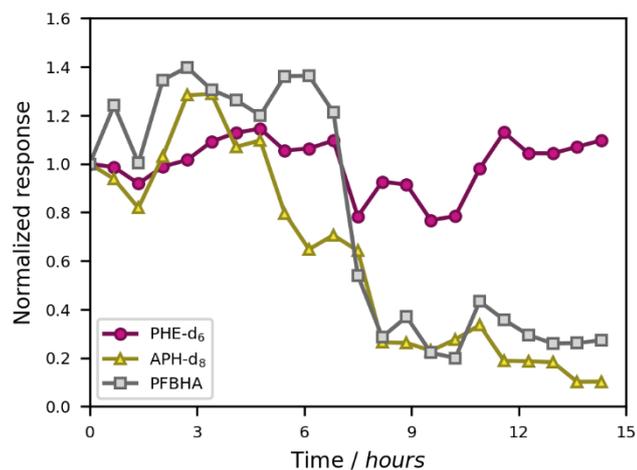
Figure S10: SPME-GC-MS data of the ISTD permeation source outflow mixed with zero air over a time frame of 15 hours. Time series of the two ISTDs and PFBHA as the carbonyl reagent are shown. Responses were normalized to the respective start value for scalability. The silylants MSTFA and TMCS were not monitored to avoid stress on the MS detector.

S6.3 Method Limitations

For the purpose of characterizing the BATCH Teflon chamber, we focused on the compounds with the best sensitivity and suitability for the on-line analysis with our setup. The compounds which we excluded after initial testing are listed in Table S9. We observed the following limitations:

Firstly, we excluded small compounds with MW < 50 g mol^{-1} (acetaldehyde, formaldehyde, formic acid, and methanol) from our method due to low sensitivity. This is in agreement with the study by Gómez Alvarez and Valcárcel (2009), where the response of formaldehyde and acetaldehyde was lower than that of benzaldehyde. Generally, PDMS/DVB fibres are designed for molecular weights in the range of MW = 50 − 300 g mol^{-1} (manufacturer specification), explaining this observation.

Secondly, most tested carboxylic acids (acetic acid, formic acid, glutaric acid, glyoxylic acid, oxalic acid, succinic acid) could only be detected at elevated sampling temperature of 85 °C due to their low volatility. This was shown by offline measurements of heated vials containing a calibration standard. Meanwhile, benzoic acid and pyruvic acid could be calibrated for on-line analysis reasonably well, possibly due to their aromaticity and additional keto group, respectively. Similar to sticky compounds such as glyoxal (see main text), we acknowledge that the on-line analysis of low-volatility compounds in the chamber could be enhanced by a different material, length, and temperature of the transfer line, and a non-interrupted flow.

Thirdly, we observed low sensitivities and poor transportation from the chamber to the instrument for ketones. This is in line with the lower affinity of ketones to PFBHA compared to aldehydes (Jang and Kamens, 1999), and additionally suggests a substantial stickiness of these compounds. We excluded non-aromatic compounds with only keto functional groups (acetone, dimethylglyoxal). For the aromatic ketones, we could use acetophenone-d$_8$ as an internal standard but excluded *p*-toluquinone. The analysis of acetophenone-d$_8$ profited from the fact that it was added constantly and could therefore equilibrate well, and that we specifically designed the permeation source to release enough mass for a good instrumental response (nevertheless, the variability of acetophenone-d$_8$ was higher than for phenol-d$_6$, see main text). Furthermore, the direct addition of keto groups to the aromatic ring may induce steric hindrance and thereby inhibit an effective PFBHA derivatization. All tested aromatic compounds with carbonyl groups detached from the ring or with hydroxy/carboxylic groups were successfully optimized for on-line analysis.

Table S9: List of all tested compounds which were not included in the final SPME-GC-MS method due to methodological limitations. The retention time (RT), number of peaks and selected peak, and molecular weight (MW) are given for each compound. The functional groups amenable to oxime formation (PFBHA derivatization) or silylation (MSTFA/TMCS derivatization) are denoted as aldehydes (CHO), ketones (C=O), alcohols (OH), and carboxylic acids (COOH). The selected ion monitoring (SIM) masses were selected to represent abundant masses resulting from mass shifts and fragmentations which are typical for the respective derivatization process (see Sect. S3.4). For 4-nitro-*m*-cresol and *p*-nitrotoluene, the on-line calibration could be performed successfully, however the noise exceeded the signal during the photooxidation experiments, so that these compounds were not evaluated.

Compound	RT / min	Peaks (selected)	MW / g mol^{-1}	Oxime formation	Silylation	SIM / m/z	Mass shift	Methodological difficulty
Acetaldehyde	6.57	2 (1)	44.10	$1 \times$ CHO	-	209.1	M+165	Low sensitivity
Acetic acid	-	-	60.06	-	$1 \times$ COOH	-	-	No response
Acetone	6.77	1	58.08	$1 \times$ C=O	-	223.1	M+165	Low sensitivity
Dimethylglyoxal	9.76	1	86.09	$2 \times$ C=O	-	281.1	M+195	Not detected in on-line calibration
Formaldehyde	5.09	1	30.03	$1 \times$ CHO	-	195.0	M+165	Low sensitivity
Formic acid	-	-	46.03	-	$1 \times$ COOH	-	-	No response
Glutaric acid	10.60	1	132.12	-	$2 \times$ COOH	261.1	M+72+57	Requires high temperature
Glyoxylic acid	11.4	1	74.04	$1 \times$ CHO	$1 \times$ COOH	326.1	M+195+57	Requires high temperature
Methanol	-	-	32.04	-	$1 \times$ OH	-	-	No response
Oxalic acid	7.112	1	90.04	-	$2 \times$ COOH	147.1	[fragment][a]	Requires high temperature
Succinic acid	9.50	1	118.09	-	$2 \times$ COOH	147.1	[fragment][a]	Requires high temperature
p-Toluquinone	14.46	2 (1)	122.12	$2 \times$ C=O	-	317.1	M+195	Not detected in on-line calibration
4-Nitro-*m*-cresol	12.22	1	153.14	-	$1 \times$ OH	210.1	M+57	Noise higher than signal
p-Nitrotoluene	8.20	1	137.14	-	-	137.1	[no derivatization]	Noise higher than signal

[a] *The ion m/z 147 is a typical fragment of silylated dicarboxylic acids (Pindado Jiménez et al., 2013).*

S6.4 Calibration Curves without ISTD Correction
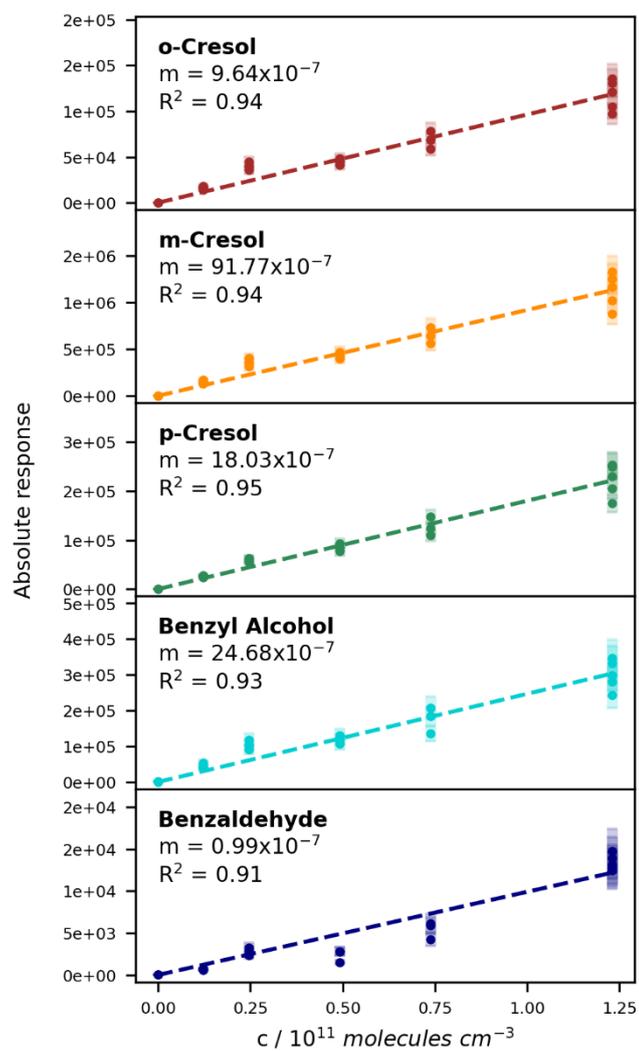
Figure S11: Calibration curves for the ring-retaining first generation products of toluene without the ISTD correction. The absolute responses are plotted against the concentration in the chamber. Uncertainty areas represent the instrumental error.

S7 Error and Validity of Loss Corrections

In order to obtain a weighted error for the loss-corrected data, we first calculated the absolute error of each loss process for each data point and compound. To do so, we considered the absolute loss, the error of the loss process, and the quantification error of the measured concentration. We then added the absolute errors of the non-corrected concentrations and the three losses to get a sum absolute error. This error was divided by the loss-corrected concentration to get a relative value.

The variability, minima and maxima, and mean values of these relative errors of the loss-corrected concentrations are listed for all compounds measured by SPME-GC-MS in Table S10. The data were collected from all 18 experiments, including temperature and NO_x variations. The mean relative errors of the loss-corrected concentrations were between 1 % (*o*-nitrotoluene) and 20 % (*p*-methylcatechol) higher than the errors of their non-corrected concentrations. Due to the added sources of uncertainty, we observed an increase of the relative error of the loss-corrected concentrations over the course of the experiment. Still, the variability of the relative error both across all the data and between the experimental means remained below 10 % for all compounds except *p*-methylcatechol which reacts fastest with OH radicals (Table S7). Benzoic acid has a similar rate constant for reaction with OH radicals but has a higher instrumental error that dominates the overall quantification error.

Table S10: Relative errors of the loss-corrected concentrations of the SPME-GC-MS data. The mean relative error and its increase compared to the quantification error of the non-corrected concentrations are given. The range of all individual relative errors across all 18 experiments as well as their variability are listed, along with the range and variability of the experimental mean values.

Compound	Loss-corrected error		All values		Experimental means	
	Mean value / %	Increase / %	Range / %	Variability / %	Range / %	Variability / %
OCR	26	10	24 – 29	4	25 – 28	4
MCR	27	12	24 – 29	4	25 – 29	4
PCR	27	11	25 – 29	4	26 – 29	3
BOH	25	8	23 – 27	3	24 – 27	3
ONT	22	1	21 – 23	1	22 – 23	1
NMB	22	3	18 – 34	8	20 – 26	6
MNT	22	2	14 – 23	5	20 – 22	3
BAC	40	7	38 – 47	3	38 – 41	2
PMC	30	20	26 – 103	32	27 – 46	14
GAL	25	5	24 – 29	3	25 – 26	2
NCR	26	5	23 – 30	4	24 – 28	3
PAC	30	18	27 – 40	9	28 – 35	6
BAL	51	9	48 – 56	3	50 – 52	1
GLY	60	6	57 – 64	2	58 – 61	1
MGL	52	10	48 – 58	3	49 – 53	2
PHB	35	8	32 – 38	4	34 – 37	3

In order to evaluate and validate the loss correction procedure at the two instruments, we compared the measured and the loss-corrected data sets obtained by SPME-GC-MS and PTR-ToF-MS. Since the extent of the loss corrections depends on the non-corrected concentrations, we selected experiments in which the measured data of the two instruments agreed particularly well. We show this comparison for benzaldehyde as a compound with no known spectral interference and high photolytic losses (Fig. S12), and for o-cresol as one of the C_7H_8O isomers and a compound with a high reactivity towards OH radicals and a relatively high wall loss rate (Fig. S13). The loss-corrected data are in good agreement.
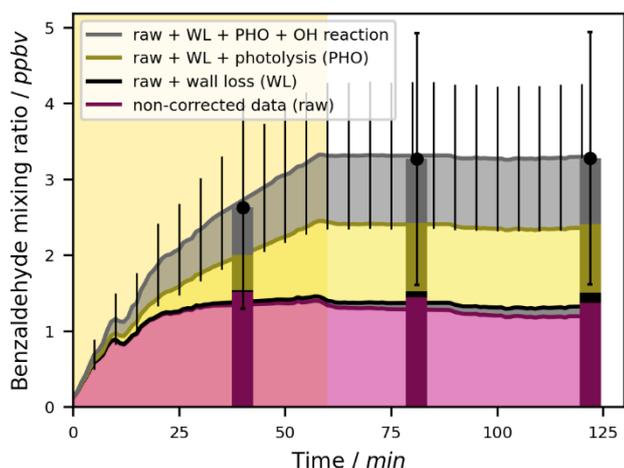
Figure S12: Measured and loss-corrected mixing ratios of benzaldehyde as obtained by the SPME-GC-MS and the PTR-ToF-MS. The data are shown for an experiment with 25 ppbv initial NO at T = 298±1 K.
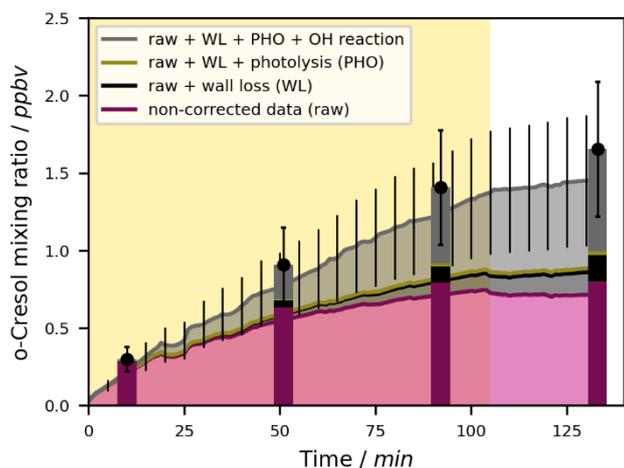
Figure S13: Measured and loss-corrected mixing ratio of o-cresol as obtained by the SPME-GC-MS and the PTR-ToF-MS. The data are shown for experiment Tol-OH-6. The mixing ratio of o-cresol at the PTR-ToF-MS was calculated from the weighted calibration and the fixed relative abundance of the C_7H_8O isomers (0.71 for o-cresol).

References

Atkinson, R., Aschmann, S. M., Arey, J., and Carter, W. P. L.: Formation of ring-retaining products from the OH radical-initiated reactions of benzene and toluene, Int. J. Chem. Kinet., 21, 801–827, https://doi.org/10.1002/kin.550210907, 1989.

Bacher, C., Tyndall, G. S., and Orlando, J. J.: The Atmospheric Chemistry of Glycolaldehyde, J. Atmospheric Chem., 39, 171–189, https://doi.org/10.1023/A:1010689706869, 2001.

Bejan, I., Aal, Y. A. E., Barnes, I., Benter, T., Bohn, B., Wiesen, P., and Kleffmann, J.: The photolysis of ortho-nitrophenols: a new gas phase source of HONO, Phys. Chem. Chem. Phys., 8, 2028–2035, https://doi.org/10.1039/B516590C, 2006.

Bejan, I., Barnes, I., Olariu, R., Zhou, S., Wiesen, P., and Benter, T.: Investigations on the gas-phase photolysis and OH radical kinetics of methyl-2-nitrophenols, Phys. Chem. Chem. Phys., 9, 5686–5692, https://doi.org/10.1039/B709464G, 2007.

Borrás, E., Tortajada-Genaro, L. A., Ródenas, M., Vera, T., Speak, T., Seakins, P., Shaw, M. D., Lewis, A. C., and Muñoz, A.: On-line solid phase microextraction derivatization for the sensitive determination of multi-oxygenated volatile compounds in air, Atmospheric Meas. Tech., 14, 4989–4999, https://doi.org/10.5194/amt-14-4989-2021, 2021.

Chen, J., Wenger, J. C., and Venables, D. S.: Near-Ultraviolet Absorption Cross Sections of Nitrophenols and Their Potential Influence on Tropospheric Oxidation Capacity, J. Phys. Chem. A, 115, 12235–12242, https://doi.org/10.1021/jp206929r, 2011.

El Dib, G., Chakir, A., Roth, E., Brion, J., and Daumont, D.: Study of Benzylperoxy Radical Using Laser Photolysis: Ultraviolet Spectrum, Self-Reaction, and Reaction with HO_2 Kinetics, J. Phys. Chem. A, 110, 7848–7857, https://doi.org/10.1021/jp056860p, 2006.

Etzkorn, T., Klotz, B., Sørensen, S., Patroescu, I. V., Barnes, I., Becker, K. H., and Platt, U.: Gas-phase absorption cross sections of 24 monocyclic aromatic hydrocarbons in the UV and IR spectral ranges, Atmos. Environ., 33, 525–540, https://doi.org/10.1016/S1352-2310(98)00289-1, 1999.

Gómez Alvarez, E. and Valcárcel, M.: Research into conditions of quantitivity in the determination of carboniles in complex air matrices by adsorptive solid phase microextraction, Talanta, 77, 1444–1453, https://doi.org/10.1016/j.talanta.2008.09.044, 2009.

Harrison, J. C. and Wells, J. R.: Gas-phase chemistry of benzyl alcohol: Reaction rate constants and products with OH radical and ozone, Atmos. Environ., 43, 798–804, https://doi.org/10.1016/j.atmosenv.2008.11.001, 2009.

Horowitz, A., Meller, R., and Moortgat, G. K.: The UV–VIS absorption cross sections of the α-dicarbonyl compounds: pyruvic acid, biacetyl and glyoxal, J. Photochem. Photobiol. Chem., 146, 19–27, https://doi.org/10.1016/S1010-6030(01)00601-3, 2001.

IUPAC: Evaluated Kinetic Data, International Union of Pure and Applied Chemistry (IUPAC) Task Group on Atmospheric Chemical Kinetic Data Evaluation, https://iupac.aeris-data.fr/ (last access 05 February 2024), 2024.

Jang, M. and Kamens, R. M.: Newly characterized products and composition of secondary aerosols from the reaction of α-pinene with ozone, Atmos. Environ., 33, 459–474, https://doi.org/10.1016/S1352-2310(98)00222-2, 1999.

Jaoui, M., Kleindienst, T. E., Lewandowski, M., and Edney, E. O.: Identification and Quantification of Aerosol Polar Oxygenated Compounds Bearing Carboxylic or Hydroxyl Groups. 1. Method Development, Anal. Chem., 76, 4765–4778, https://doi.org/10.1021/ac049919h, 2004.

Johnston, H. S., Davis, H. F., and Lee, Y. T.: NO_3 Photolysis Product Channels: Quantum Yields from Observed Energy Thresholds, J. Phys. Chem., 100, 4713–4723, https://doi.org/10.1021/jp952692x, 1996.

Kahan, T. F., Washenfelder, R. A., Vaida, V., and Brown, S. S.: Cavity-Enhanced Measurements of Hydrogen Peroxide Absorption Cross Sections from 353 to 410 nm, J. Phys. Chem. A, 116, 5941–5947, https://doi.org/10.1021/jp2104616, 2012.

Lai, Z. and Fiehn, O.: Mass spectral fragmentation of trimethylsilylated small molecules, Mass Spectrom. Rev., 37, 245–257, https://doi.org/10.1002/mas.21518, 2018.

Meller, R., Raber, W., Crowley, J. N., Jenkin, M. E., and Moortgat, G. K.: The UV-visible absorption spectrum of methylglyoxal, J. Photochem. Photobiol. Chem., 62, 163–171, https://doi.org/10.1016/1010-6030(91)87017-P, 1991.

Mellouki, A. and Mu, Y.: On the atmospheric degradation of pyruvic acid in the gas phase, J. Photochem. Photobiol. Chem., 157, 295–300, https://doi.org/10.1016/S1010-6030(03)00070-4, 2003.

Mitchell, G. D.: A Review of Permeation Tubes and Permeators, Sep. Purif. Methods, 29, 119–128, https://doi.org/10.1081/SPM-100100005, 2000.

Namies´nik, J.: Generation of standard gaseous mixtures, J. Chromatogr. A, 300, 79–108, https://doi.org/10.1016/S0021-9673(01)87581-6, 1984.

Olariu, R. I., Barnes, I., Becker, K. H., and Klotz, B.: Rate coefficients for the gas-phase reaction of OH radicals with selected dihydroxybenzenes and benzoquinones, Int. J. Chem. Kinet., 32, 696–702, https://doi.org/10.1002/1097-4601(2000)32:11<696::AID-KIN5>3.0.CO;2-N, 2000.

Pindado Jiménez, O., Pérez Pastor, R. M., Vivanco, M. G., and Santiago Aladro, M.: A chromatographic method to analyze products from photo-oxidation of anthropogenic and biogenic mixtures of volatile organic compounds in smog chambers, Talanta, 106, 20–28, https://doi.org/10.1016/j.talanta.2012.11.081, 2013.

Reed Harris, A. E., Doussin, J.-F., Carpenter, B. K., and Vaida, V.: Gas-Phase Photolysis of Pyruvic Acid: The Effect of Pressure on Reaction Rates and Products, J. Phys. Chem. A, 120, 10123–10133, https://doi.org/10.1021/acs.jpca.6b09058, 2016.

Roth, E., Chakir, A., and Ferhati, A.: Study of a Benzoylperoxy Radical in the Gas Phase: Ultraviolet Spectrum and $C_6H_5C(O)O_2$ + HO_2 Reaction between 295 and 357 K, J. Phys. Chem. A, 114, 10367–10379, https://doi.org/10.1021/jp1021467, 2010.

Sandus, O. and Slagg, N.: Reactions of Aromatic Nitrocompounds. 1. Photochemistry, Feltman Research Laboratory, Picatinny Arsenal, Dover, NJ, 1972.

Šepič, E. and Leskovšek, H.: Isolation and identification of fluoranthene biodegradation products, Analyst, 124, 1765–1769, https://doi.org/10.1039/A904990H, 1999.

Serralheiro, C., Duflot, D., da Silva, F., Hoffmann, S., Jones, N., Nj, M., B, M., and P, L.-V.: Toluene Valence and Rydberg Excitations as Studied by ab initio Calculations and Vacuum Ultraviolet (VUV) Synchrotron Radiation, J. Phys. Chem. A, 119, https://doi.org/10.1021/acs.jpca.5b05080, 2015.

Shama, S. A. A. E.-A.: Vacuum ultraviolet absorption spectra of organic compounds in gaseous and liquid state, Doctoral thesis, University of Zagazig, Zagazig, 1991.

Thorenz, U. R., Kundel, M., Müller, L., and Hoffmann, T.: Generation of standard gas mixtures of halogenated, aliphatic, and aromatic compounds and prediction of the individual output rates based on molecular formula and boiling point, Anal. Bioanal. Chem., 404, 2177–2183, https://doi.org/10.1007/s00216-012-6202-5, 2012.

Troe, J.: Are Primary Quantum Yields of NO_2 Photolysis at $\lambda \leq 398$ nm Smaller than Unity?, Z. Für Phys. Chem., 214, 573, https://doi.org/10.1524/zpch.2000.214.5.573, 2000.

US EPA: Estimation Programs Interface Suite (EPI Suite), model AopWin v1.92, United States Environmental Protection Agency, 2024.

Volkamer, R., Spietz, P., Burrows, J., and Platt, U.: High-resolution absorption cross-section of glyoxal in the UV–vis and IR spectral ranges, J. Photochem. Photobiol. Chem., 172, 35–46, https://doi.org/10.1016/j.jphotochem.2004.11.011, 2005.

Wu, C., De Visscher, A., and Gates, I. D.: Reactions of hydroxyl radicals with benzoic acid and benzoate, RSC Adv., 7, 35776–35785, https://doi.org/10.1039/C7RA05488B, 2017.

Zhu, L. and Cronin, T. J.: Photodissociation of benzaldehyde in the 280–308 nm region, Chem. Phys. Lett., 317, 227–231, https://doi.org/10.1016/S0009-2614(99)01375-5, 2000.